

Water Resources Research®

RESEARCH ARTICLE

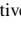



10.1029/2021WR030107

Hydrodynamic Modeling of Inundation Patterns of a Large African Floodplain Indicates Sensitivity to Waterway Restoration



Key Points:

- Large floodplains are hydrodynamically sensitive to relatively modest changes
- Modifications of the floodplain have influenced the timing and distribution of floodwaters
- A robust modeling approach is created through a multiobjective function and time slice calibration approach

T. D. M. Willis¹ , M. W. Smith¹, D. E. Cross² , A. J. Hardy³ , G. E. Ettrich³, H. Malawo⁴, C. Chalo⁴, M. Sinkombo⁴, and C. J. Thomas⁵ 

¹School of Geography and Water, University of Leeds, Leeds, UK, ²Institute of Biological, Environmental and Rural Sciences, Aberystwyth University, Aberystwyth, UK, ³Department of Geography and Earth Sciences, Aberystwyth University, Aberystwyth, UK, ⁴Zambia Water Resources Management Authority (WARMA) Mongu Office, Mongu, Zambia, ⁵Lincoln Centre for Water & Planetary Health, University of Lincoln, Lincoln, UK

Correspondence to:

T. D. M. Willis,
t.d.willis@leeds.ac.uk

Citation:

Willis, T. D. M., Smith, M. W., Cross, D. E., Hardy, A. J., Ettrich, G. E., Malawo, H., et al. (2022). Hydrodynamic modeling of inundation patterns of a large African floodplain indicates sensitivity to waterway restoration. *Water Resources Research*, 58, e2021WR030107. <https://doi.org/10.1029/2021WR030107>

Received 9 APR 2021
Accepted 6 NOV 2022

Author Contributions:

Conceptualization: M. W. Smith, D. E. Cross, A. J. Hardy, G. E. Ettrich, C. J. Thomas

Data curation: D. E. Cross, H. Malawo, C. Chalo, M. Sinkombo

Formal analysis: H. Malawo, C. Chalo, M. Sinkombo

Methodology: M. W. Smith

Writing – original draft: M. W. Smith

Writing – review & editing: D. E. Cross, A. J. Hardy, G. E. Ettrich, C. J. Thomas

Abstract Large-scale floodplains are important features of the African continent. Regular inundation provides the means to support large populations but can also present problems such as access to health facilities and water body formation that sustain malaria vectors. Modeling of these floodplains is therefore important, but complex. In this research, we develop, calibrate, and validate a hydrodynamic model of the Barotse Floodplain, of the Upper Zambezi, Zambia. The floodplain has seen recent infrastructure developments including the restoration of the canal network and construction of a cross floodplain causeway. In order to create a robust model, a multiobjective calibration uses a time slice approach based on available Landsat satellite image overpasses. An emulator-based sensitivity analysis indicates the significance of hydrological processes in the model. Model evaluation is undertaken for two events in the gauge record (2009 and 2018), of similar magnitude that occur before and after modifications to the floodplain. Results indicate a complex impact of infrastructure development on the hydrodynamics of the floodplain, with a higher peak flow, but with a redistribution of water throughout the floodplain. Deeper flooding is observed in some areas while others experience lower water levels. The sensitivity results also reflect a change in processes, where floodplain flows dominate the 2009 event, whilst channel process dominate the 2018 event. Overall, we show that relatively modest modifications to the floodplain have impacted flood water levels, which in turn will influence access route availability and alter malaria transmission rates.

1. Introduction

Floodplains have long been a focus for human occupation across the world covering more than 2×10^6 km² (Tockner & Stanford, 2002), providing homes and livelihoods for hundreds of millions of people throughout Africa (Dunne & Aalto, 2013; Leauthaud et al., 2013; Rebelo et al., 2010). Although floods are hazardous to property and human lives, annual flood cycles provide moisture, and fertile soils upon which floodplain communities depend (Cai et al., 2017). In Zambia alone, wetlands are estimated to contribute around 5% of gross domestic product (GDP), disproportionately supporting the poorest people (IWMI, 2014).

Over recent decades, changing hydrological dynamics of large African wetlands has threatened the traditional systems of living alongside floods (e.g., Zimba et al., 2018). It is expected that these changes will be amplified in a warming climate, with Alfieri et al. (2017) estimating that a 4° rise in global temperatures could result in a 500% increase in flood risk for 70% of the global population. In the Barotse floodplain in Zambia, for example, flood magnitudes have increased but the timing of the peak flood has also become more variable (Cai et al., 2017), damaging food and income sources and challenging existing land use practices.

Floods also have serious effects on health systems (Schatz, 2008). The large floodplains of sub-Saharan Africa are especially vulnerable, as the ratio of people to health facilities can be 1:50,000 (Faruk et al., 2020). Changing floodplain inundation dynamics affects this already challenging health service access. Moreover, local disease dynamics (e.g., diarrhea, cholera, malaria) are influenced by the presence and persistence of floodwater in proximity to human settlements. With 93% of global malaria cases reported in sub-Saharan Africa intrinsically linked to water bodies via the breeding habitat of the Anopheles mosquito vector, understanding the location and timing

© 2022. The Authors.

This is an open access article under the terms of the [Creative Commons Attribution License](https://creativecommons.org/licenses/by/4.0/), which permits use, distribution and reproduction in any medium, provided the original work is properly cited.

of floodplain inundation both at present and in the future is critical to building climate resilient health systems (WHO, 2019).

Recent efforts have focused on providing accurate maps of surface water body availability using radar satellite data (e.g., Hardy et al., 2019) to assist the targeting of disease control interventions. However, these important contributions offer no predictive capacity required to inform agricultural practices, malaria control activities or health system plans. The impact of changing hydrometeorological conditions in sub-Saharan Africa is difficult to assess given the nonlinear relationship between flood hazard and rainfall anomalies (Coughlan de Perez et al., 2017; Stephens et al., 2015) resulting in observed changes in flood timing that are larger than variability in rainy season onset and duration (Ficchi & Stephens, 2019). Yet, hydrological observations remain sparse in large African floodplains (Cai et al., 2017; Zimba et al., 2018) which presents challenges for the application of hydrodynamic models to simulate flood dynamics over such large landscapes.

Global Flood Models (GFMs) can provide a broad indication of changing flood hazards across large areas. However, an intercomparison exercise of GFMs showed considerable variability in estimates across Africa (Trigg et al., 2016) and early validation efforts indicate that flat extensive floodplains are especially challenging to model correctly (Bernhofen et al., 2018). Such global models are currently limited in what they can be used to predict (Ward et al., 2013) and are based on relatively coarse global terrain data (Yamazaki et al., 2017). Hydrological processes are not integrated into hydrodynamic calculations but rather included in the boundary conditions and often based on synthetic approaches (Grimaldi et al., 2013, 2019; Pappenberger et al., 2012; Sampson et al., 2015; Wing et al., 2017). GFMs necessarily overlook local hydrological processes that can be significant for local inundation dynamics (Rajib et al., 2020).

More accurate simulations of the annual inundation of floodplains are achievable using 2D hydraulic models. Recently, several studies have used the 2D-simplified hydrodynamic model LISFLOOD-FP (Bates et al., 2010; Neal et al., 2012) to model fluvial flooding patterns over large African floodplains, including the Logone floodplain in Cameroon (Shastry et al., 2020), the Oti River in West Africa (Komi et al., 2017), and the Congo in the Democratic Republic of the Congo (O'Loughlin et al., 2020). While satellite remote sensing of flood extents permits model calibration based on flood extent, data availability remains a challenge both for model setup and calibration and the ability of many standard methods to identify vegetated water bodies accurately is limited, as demonstrated for the Barotse floodplain in Western Zambia by Hardy et al. (2019). The focus of previous models has been on simulating the flood peak with models optimized for replicating maximum flood extents, while the applications identified above, especially estimation of the spatiotemporal variability in *Anopheles* mosquito vector habitats, require simulation of the full annual flood cycle. The same requirements can also be used in understanding healthcare facility access. Studies that have explored the calibration of hydrodynamic models throughout the flood cycle using multiple data sets, have demonstrated both the complexity of achieving such a simulation and the need for further research into developing models for this purpose (e.g., over the Amazon (Pinel et al., 2020; Rudorff et al., 2014) and Mekong (Dung et al., 2011) rivers).

The aim of this study is to determine the dominant hydrological processes of the Barotse Floodplain (Western Zambia) through the development of a hydrodynamic model designed to model the annual flood cycle. Model calibration is based on both river gauge data and observed satellite inundation extents over multiple time slices covering both the flood peak and the flood drawdown period. A global sensitivity analysis is then used to indicate the significance of each model parameter and thereby improve our understanding of both floodplain processes and the modelling of these processes (Beven, 2007). Using the knowledge gained from the model, the effect of recent floodplain modifications, specifically the construction of a causeway and dredging of canals funded by the World Bank Climate Investment Fund, on the floodplain hydrodynamics will be evaluated. These will be evaluated in the context of changes to the peak flows and extents but also the length of time that regions in the floodplain remain inundated, which links to other local management priorities of malaria vector habitat formation and healthcare access.

2. Barotse Floodplain

The Barotse Floodplain is a major hydrological feature of the Upper Zambezi river system. The region, a designated Ramsar site, is dominated by grasslands, overlaying a deep layer of Saharan sands (Ramsar, 2007). The floodplain is 250 km long and 50 km wide, with an extremely low downstream gradient; the elevation difference

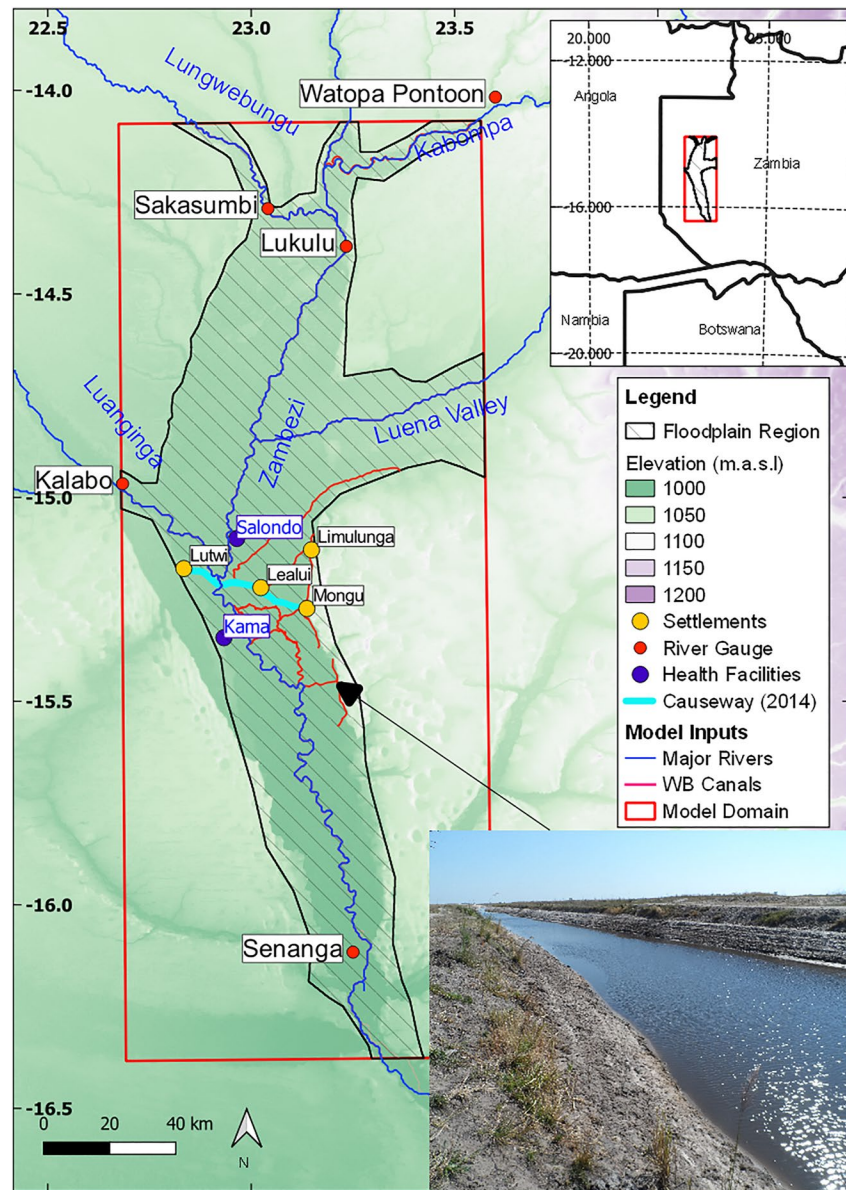


Figure 1. Barotse Floodplain with the locations of the model domain, main river network, canals, causeway, and selected health facilities. Background elevation shading is derived from TanDEM-X1 terrain data. Inset: an example of a restored canal with the location highlighted on the main map.

along the north-south valley axis is just 30 m. At the northern point of the floodplain, the Zambezi drains a catchment of around 300,000 km², while several tributaries including the Luangvinga and Luena Rivers have a confluence with the Zambezi in the Barotse floodplain (Figure 1). The wet season typically lasts from November to January driven by rainfall from the north-south movement of the Intertropical Convergence Zone (ITCZ). The floodplain is flooded annually, with the typical annual flood cycle characterized by a discharge minimum in September, the onset of flooding in early March, peak discharge in April and a return to in-channel flow occurring by early June (Ramsar, 2007). However, flood waters persist well beyond the flood recession within disconnected negative relief assemblages that are characteristic of large river floodplains (Lewin & Ashworth, 2014). Due to the low gradient the floodwaters move slowly through the floodplain, with relatively few topographic features to impede flow paths.

The regularity of the flooding dominates the lives of the local inhabitants of the floodplain with seasonal movements of people and villages to and from high ground occurring around the onset and recession of the flooding

(Cai et al., 2017). Recent development and modification of the floodplain includes the construction of the Mongu-Lutwi causeway in 2014, the first large scale and permeant infrastructure in the floodplain, containing 26 bridges and spanning the width of the floodplain. The floodplain canal network has also been modified. Traditionally, this activity was undertaken by local communities (Chikozho & Mapedza, 2017) but canal maintenance has reduced in recent years, and many channels became inaccessible (The World Bank, 2010). As part of funding by the Climate Investment Funds initiative, in 2014, the World Bank restored 250 km of canals in the floodplain that had become unusable (BRLi and NIRAS, 2014), and has restored canal access to large parts of the floodplain.

Hydrological modeling of the Upper Zambezi catchment using the Soil and Water Assessment Tool (SWAT; Arnold et al., 1998) and semidistributed HBV (Lindström et al., 1997) rainfall-runoff models have been undertaken previously to investigate water resourcing problems (Cohen Liechti et al., 2014; Kling et al., 2014) and to evaluate the use of radar altimetry in river monitoring (Michailovsky and Bauer-Gottwein., 2014). The changing patterns of floodplain inundation extents through time was recently investigated by Zimba et al. (2018), by coupling MODIS and LandSAT 8 remote sensing data with river gauge data. Flow gauge data indicated a downward trend of floodwater volume through the period 1954 to 2004, with the pattern of rainfall in the upper catchment and evaporation rates in the floodplain identified as the drivers for annual variations in floodplain water volume and the timing of inundation.

3. Methodology

The Barotse floodplain hydraulic model was developed in two phases. First, a general model configuration phase was used to identify the key hydrological processes to be included (Section 3.1). Once the basic model configuration was determined, the model was calibrated and validated based on the parameters selected from the first phase, and using multiple model evaluation functions. This included a time slice observed water extent approach, where multiple overpasses from the optical LandSAT 8 satellite imagery archive are used to evaluate model output, alongside gauge data (Section 3.2). In order to understand the calibration/validation model results, a variance-based sensitivity analysis phase was then undertaken to quantify the impact of the input parameters on model results (Section 3.3). Finally, the calibrated hydraulic model was used as the basis for a high-resolution model capable of replicating more detailed processes in the floodplain (Section 3.4), and to evaluate the impact of the modifications to the floodplain.

To assess the impact of the modifications to the floodplain, two annual events (2009 and 2018) are used in the calibration, validation and sensitivity tests which provide similar values of peak discharge before and after floodplain modifications (Figure 2). These events were among the largest in the Lukulu gauge record that are contemporaneous with cloud-free LandsAT imagery that cover similar points in the flood cycle. For both events, all sets of simulations defined for the calibration are used to understand how modifications to the floodplain have altered both the calibrated values and the significance of each parameter on model results, thereby extending beyond a simple validation exercise.

3.1. Model Configuration

The model configuration stage was used for three purposes; identifying data sets and models for the study, identifying the important parameters and inputs of the model, and creating value ranges for those parameters with which to calibrate and validate the model. Broadly, the main parameters to be calibrated were Manning's n for channel and floodplain, infiltration rates of the soil, evaporation rates from the floodplain, and the depth of the river channel. For each parameter, we introduce a sampling distribution based on the ranges of values for the parameter which are used in the selecting values for calibration and validation. These can be seen in Table 1.

Floodplain hydraulics were modeled using the LISFLOOD-FP hydrodynamic model (Bates & De Roo, 2000; Trigg et al., 2009). Floodplain flow is modeled with the “acceleration” formulation, a simplified version of the governing shallow water equations (Bates et al., 2010). In this floodplain calculation formulation, the local convective term is dropped from the governing equations and can be used when the hydraulic conditions are dominated by low velocity subcritical flow (Neal et al., 2012). In these situations, the uncertainty associated with the numerical model has no greater impact to overall model results than uncertainties associated with other model inputs (Willis et al., 2019). LISFLOOD-FP also contains multiple methods for determining channel flow in the river network: an integrated 1D model that uses the diffusion approximation of the shallow water equations

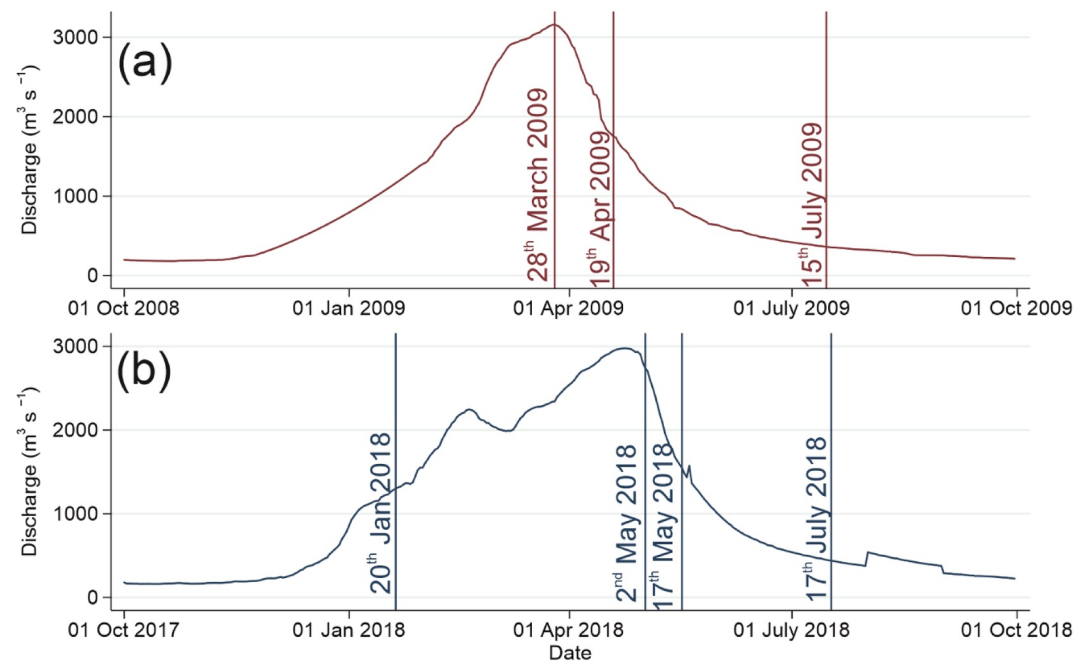


Figure 2. Hydrographs for the Lukulu river gauge for the River Zambezi for the (a) 2009 and (b) 2018 annual flood events with corresponding LandSAT-based model evaluation points indicated.

(Bates & De Roo, 2000) and a subgrid channel method that represents channel flow as a component of the intercell flux calculation (Neal et al., 2012). A recent study using LISFLOOD-FP to model the hydraulics of an African floodplain successfully used the subgrid approach (Shastry et al., 2020), so both approaches to representing channel flow were tested in this study at the low resolution and high resolution. While both approaches performed sufficiently well at the low resolution, it was found that the 1D channel method was better at capturing the drying of the floodplain in the recession phase of an event for high resolution simulations, and was selected to represent the channel in this study. The 1D approach does have a compromise in the linking of the Little Zambezi to the main Zambezi channel, requiring flow to pass between the 2D domain, before reentering the 1D domain. This compromise was considered less critical than the ability of the overall model to replicate the flow patterns throughout the year. Considering the ability of the subgrid approach to perform at a high standard in other floodplains, the selection of the 1D model may be specific to this location.

The dimensions of the model domain were determined based on the location of major rivers, channels, and river gauge locations (Figure 1). In order to capture the full range of flood mechanisms for the Barotse, the model domain was extended to include the Kabompo and Lungwebungu channels. TanDEM-X1 terrain data (from 2016) (Wessel et al., 2018) was selected for high-resolution floodplain terrain data. The terrain data are derived from interferometric synthetic aperture radar (InSAR) which has base resolution of 0.4 arc sec (~12 m) and a vertical accuracy rating for floodplain of ~2 m (Wessel et al., 2018). The terrain data are filtered for noise, vegetation, and water, using imagery segmentation (Shepard et al., 2019) to create a Digital Terrain Model (DTM) for use as the input to the model. As the region is dominated by grass with a consistent year-round coverage,

Table 1
Parameters and Sample Range for the Model Inputs in the Calibration/Validation and Sensitivity Analysis

Parameter	Range	Distribution
Floodplain n	0.01–0.06	Uniform
Channel n	0.01–0.03	Uniform
Infiltration (mm h^{-1})	0.2–20	Uniform
Evaporation (mm d^{-1})	3.4–6.6	Gaussian (mean = 4.8)
Channel Depth (m)	3.5–5.5	Gaussian normal, based on bathymetry data

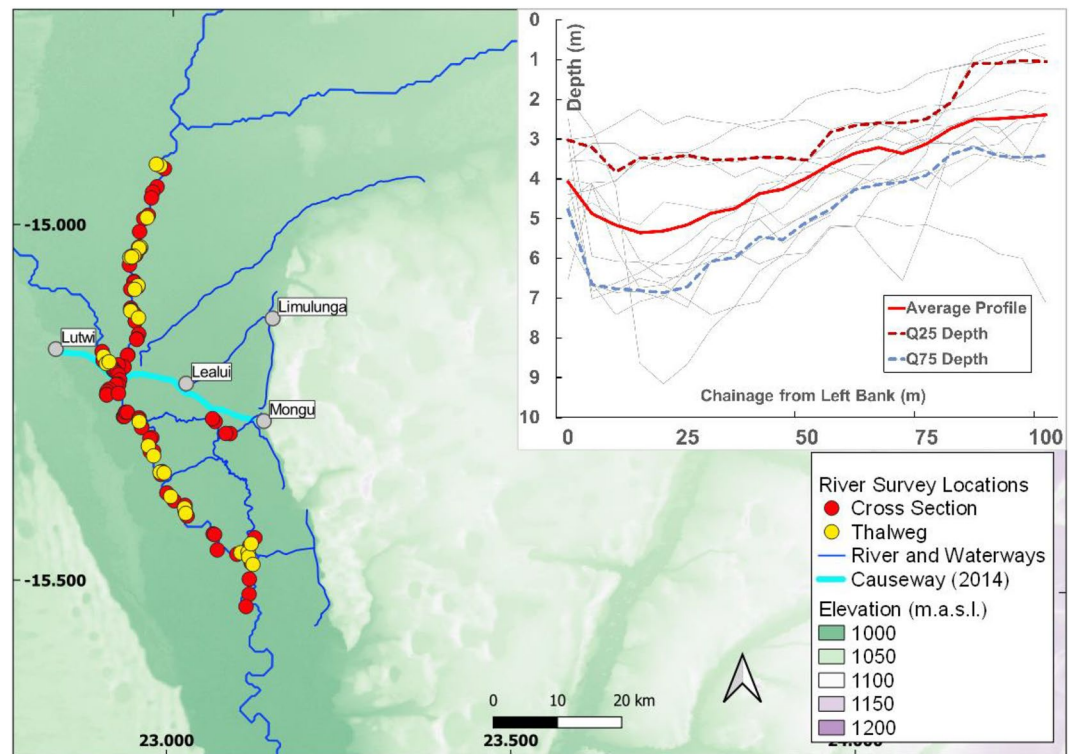


Figure 3. Location of the river cross sections and thalweg sampling locations. River cross sections are shown and summarized in the inset graph.

with typical heights of 10–20 cm, issues relating to errors caused by vegetation are assumed to be less significant than other errors in the model input data. The suitability of [TanDEM Data](#) in hydraulic flood modeling has been established by Archer et al. (2018), although it was highlighted that more robust data smoothing techniques are required. The results presented here should be considered within this context.

Terrain data were sampled to 900 m for the calibration simulations and resampled to 100 m for high resolution model runs. The motivation behind this approach is computational cost. The 900 m model run completes an event in around 1%–2% of the time the 100 m model, ensuring that more simulations can be completed and a more comprehensive calibration exercise completed. We stress that this approach is applicable in this study, based on the assumptions that the main hydrodynamic processes will be relatively independent of the cell size, due to the underlying topography (low slope with no significant macrotopographical features), and the low velocity nature of the flood events. The same approach could not be used in more complex hydrological environments. This assumption is justified here via the similar performance of the 100 and 900 m models when compared against the observed data for both 2009 and 2018 events.

Bathymetric data were collected from a 40 km stretch of the river (Figure 3). These data were used in the high-resolution 1D model and the depth parameter for the sub-grid model, which defines the depth of the channel for both the subgrid model (Neal et al., 2012). The bathymetric data were collected from a Garmin EchoMap chirp 45cv depth sounding sonar mounted to a Bayliner 170 boat. GPS coordinates were used to map the location of the depth points. A total of 50 cross sections and 20 thalweg (longitudinal) sections were collected from the main river network, including the main Zambezi channel the Luanginga tributary, and some of the anabranch channels as can be seen in Figure 3. Cross section sample locations were selected to include meanders and straight sections of river. A consistent low speed (around 8 km hr⁻¹) was maintained to ensure a constant bow profile for the boat and consistent measurements. On average, 35 sample points were taken for each cross section, with a spatial resolution of around 10 m. Thalweg sections were sampled at meanders and straight sections, with the precise location of the sample sections based on assumptions of dominant flow paths in channels. Each section was surveyed with the same approach and resolution as the cross sections, with lengths of samples ranging from 500 m to 1.8 km.

Broadly, the main channel ranged in a maximum depth of between 3.6 and 5 m. A bathymetric model was created from these survey data (Figure 3). In the absence of a complete survey, these data were used to define a constant channel depth for the whole reach, the value of which was calibrated based on sampling possible depths from the bathymetric model. The range of depths were sampled from a normal distribution based on the field measurements. Initial water depths in the channel were also considered and included in the calibration, but were shown to be insignificant to model performance.

River flow data were used as inflow boundary conditions. These were determined from the Water Resources Management Authority (WARMA) river gauges (Figure 1) that record daily maximum depths with a discharge value, estimated from a rating curve calculation. The main inflow to the model region comes through the Lukulu gauge, which records flow on the River Zambezi and represents 85% of the total inflow to the model. Additional tributary inflows are also highlighted in Figure 1, with a further gauge in the Luena valley being located outside Figure 1. As three channels contribute flow to the Lukulu gauge, the inflow for the main channel was adjusted to account for the additional inflows from the Lungwebungu and Kabompo river.

Initial model runs were completed without water loss mechanisms but failed to capture the drawdown at the end of the event. As the Barotse Floodplain is a hydrological sink of the River Zambezi, reducing the mean annual flow by 1.5% or an annual contribution of $-17.6 \text{ m}^3 \text{ s}^{-1}$ (The World Bank, 2010), water loss mechanisms were also included. A constant infiltration approach was used which did not significantly increase model runtime and produced similar model results to a time variable approach using a range of possible rates determined from the dominant surface/subsurface material of the floodplain. In the absence of measured data, evaporation rates were derived from the Worldly 2 Global-Potential Evapo-Transpiration data set (Fick & Hijmans, 2017), which provides gridded monthly average values of potential evapotranspiration. Both infiltration and evaporation parameters were sampled from uncertainty ranges highlighted in Table 1. For both parameters, a uniform distribution was assumed due to the lack of observation data with which to evaluate other distributions.

Manning's n friction parameters for the channel and floodplain were also calibrated (Table 1). The range of values for these parameters are based on dominant land cover of the floodplain, grasslands (The World Bank, 2010), and the dominant river bank material which are predominately unmodified sand/gravel mix. The ranges are those recommended in typical Manning's n tables (e.g., Chow et al., 1988), but extended to account for additional processes in the channel that are not observable at the macroscale. In LISFLOOD-FP and other hydrodynamic models, the selected value is an effective parameter—a parameter that compensates for physical processes not included in the governing equations of numerical code in the model. Therefore, a wider range of parameters is justified to ensure good model performance. A uniform distribution is assumed for the friction to reflect the equal probabilities of all friction values being representative of the underlying conditions.

The cross-floodplain causeway was incorporated into the terrain data by increasing the elevation of cells in the causeway footprint by 6 m (except at 26 bridge locations), and setting the Manning's n value of these cells to 0.015 to reflect the concrete capping. The canal network was added to the model by modifying the 1D channel network, using design profile and depths from the Environmental and Social Impact report (BRLi and NIRAS, 2014), and used the same Manning's n value used for the main river channel network, as the canals are not modified beyond the initial dig and construction. We assume that significant geomorphic modification to the channel or floodplain has not occurred between the 2009 and 2018 events.

3.2. Model Evaluation, Calibration, and Validation

The models were assessed through two approaches. First, discharge is compared using the Nash/Sutcliffe Efficiency (NSE) coefficient at the Senanga discharge/level gauge at model outflow (Figure 1), as in Equation 1:

$$NSE = 1 - \frac{\sum_{i=1}^n (o_i - m_i)^2}{\sum_{i=1}^n (o_i - \bar{o})^2} \quad (1)$$

where m is model data set, o is observed data, i is a time index and \bar{o} is the average observed discharge value. NSE varies between 1 and $-\infty$, where one is an exact match between modeled and observed discharge.

The second approach compares the modeled flood extent to the observed flood extent, extracted from LandSAT satellite data resampled to the model resolution using a nearest neighbor method. Comparison is made the using

the F^2 goodness of fit measure, also known as the CSI index (Aronica et al., 2002). The F^2 measure is a ratio of the region or number of cells where both modeled data m and observed data o coincide (either flooded or nonflooded) and the region or number of cells where the model and observed differ, as in Equation 2:

$$F^2 = \frac{\sum(m_1^{ij} o_1^{ij}), (m_0^{ij} o_0^{ij})}{\sum(m_1^{ij} o_1^{ij}), (m_0^{ij} o_0^{ij}), (m_0^{ij} o_1^{ij}), (m_1^{ij} o_0^{ij})} \quad (2)$$

where m is model data set, o is observed data, and ij is a cell reference. The F^2 value varies between 1 and 0, where one is an exact match between modeled and observed flooded cells.

LandSAT-derived water body extents were extracted using the Normalized Difference Waterbody Index (NDWI). For both the 2009 and 2018 events, multiple overpasses occur with complete coverage of the floodplain (see Figure 2), which allow the model to be compared at different phases of the flood cycle. Other methods to extract water bodies from imagery data sets such as the modified NDWI method (Xu, 2005) which can provide more comprehensive classifications of vegetated water were inappropriate as the majority of vegetation would be classified as wet following the end of the rainy season in January. The impact of rainfall on the overall flood waters is negligible, and using this classification would present the calibration/validation process with significant complications, as rainfall is not included in this model setup. The floodplain is also dominated by grasslands (The World Bank, 2010), rather than forest or canopy cover that might be typical to tropical floodplains. Therefore, the NDWI approach is preferred, despite the limitations, such as the inability to identify water bodies beneath tree canopies and relative age of this approach.

The causes behind variations in model performance were examined using flood inundation likelihood maps. Such maps represent the number of times an individual cell is modeled as being inundated in the range of simulations in the calibration/validation phase and offer a representation of the spatial variation in model performance. The value of cell ranges between 100% and 0%, where 100% is given when a cell has flooded in all simulations and 0% where it has not flooded in any of the simulations (Aronica et al., 2002).

Using these two-evaluation metrics for model calibration/validation, we follow the multiple-objective approach, whereby the optimal model is located within the Pareto front of sampled simulations (Dung et al., 2011). Since this approach selects a set of parameters that has a high level of performance across multiple evaluation methods (rather than a single evaluation method), this parameter set is often a compromise that performs well across all objective functions. For the calibration/validation, a systematic sampling approach was used to create a set of simulations that covered the range of values for each parameter. Four hundred samples were taken to create the simulations which were used for the calibration/validation and to construct the emulator detailed in Section 3.3. The 400 simulations were repeated for 2009 and 2018, with the parameter set that provided the optimal performance for the 2009 event being validated in the 2018 event to ensure equal response to both events from the final model. Repeating the same parameter sets for both events provides the means to explore how parameter sets change over the simulation space.

3.3. Sensitivity Analysis

Sensitivity analysis was undertaken to quantify the significance of the effect each parameter has on model results, thereby both determining how much effort needs to be considered in establishing each parameter and improving understanding of key processes in the model. Typically, variance-based approaches, such as the Sobel functions, are used to quantify the contribution of an input to model uncertainty (Hall et al., 2009, 2011), but are computationally expensive. We address this limitation through the creation of an emulator of the original computation code, based on the outputs of the model over a defined parameter space. This methodology is integrated into the Bayesian Calibration of Computational Codes, or BACCO approach (Oakley & O'Hagan, 2002) and has been used in previous studies investigating the uncertainties in calibrating hydraulic models (Hall et al., 2011). The outputs of the statistical model were mapped across a sampled input parameter space. In comparison to a full sensitivity analysis, a smaller number of simulations from the input parameter space were used with the original model to inform the emulator. From these training points a statistical approximation to the model was created, which returns the same value as the original model at the training locations while also providing a reasonable approximation to the interpolated values (with uncertainty evaluated using data points that were not used in the training process).

Once a statistical fit was achieved, the emulator was used for variance-based style sensitivity analysis, in which the contribution of a parameter to overall model variance is described in percentage terms (see Oakley & O'Hagan, 2002 for further description). The BACCO approach applied a Gaussian Process emulator, which assumed that the model responds smoothly to changes in the model inputs and that this model response was normally distributed. A structured sampling process was used to create the input parameter space based on ranges of the six parameters in Table 1. The sample size was increased until convergence of the emulator was achieved. For this study, an emulator was built for each of the objective functions, although the same model training points could be used for each. The simulations used as training points for the emulator were also used as the simulations for the calibration and validation exercise. This was possible, as the coverage of the parameter space to create a sufficiently high-quality emulator by the training points can also be assumed to provide sufficient coverage to calibrate the model, and is distinct advantage is using an emulator approach for sensitivity testing. Using a 20% cut estimate for cross validation resulted in a range of root mean square relative error values between 1.5% and 3% for all emulators.

3.4. High Resolution Model

A higher resolution 100 m model was then constructed for both 2009 and 2018 flood events to improve the representation of the causeway and canals, and also water bodies that form in the recession phase of the flood cycle. These water bodies may act as potential mosquito larval breeding sites as well as alter the accessibility of regions due to flood waters. These simulations were undertaken on the University of Leeds ARC3 High Performance Computing system, using Intel Xeon Gold nodes 6138 CPUs. The simulations are run over multiple cores, taking around 240–300 hr per flood event for the high-resolution model, and 1–3 hr for the coarse resolution model. The length of time of the simulation limited the scale at which this model could be further refined. Here high resolution is contextual, but simulations with 12 m resolution could be achieved with higher computational power. Additionally, to clarify the effects of canal modification and causeway construction, each event was run on the opposite terrain data set. Differences in flow depths and accessibility of locations via car (defined as accessible if water depth <0.3 m) are then computed.

4. Results

4.1. Model Calibration and Validation

For both the 2009 and 2018 events, the pattern of the F^2 function is similar across the year, noting that no LandSAT scenes were available for the annual flood rising limb in 2009. The highest value for both years occurs at the peak of the annual flood (F^2 values of 0.54 in March 2009 and 0.75 for May 2018). Based on the range of results produced across the total model ensemble for the calibration process, the level of uncertainty is greater at the peak flow with a range of 184% and 234% for 2009 and 2018, respectively. The range of results for each point of the time slice calibration can be seen in Figure 4.

Model performance in the rising limb phase of the event and the flood recession are low, with a narrower range of values. The July overpasses in 2009 and 2018 lead to average F^2 scores of 0.08 and 0.10, respectively. A greater range is observed for the 2009 event: 189% from minimum to maximum versus 139% in 2018. A similarly low level of performance is measured for the January 2018 overpass, but with a greater range of results (318%).

Figure 5 presents the flood inundation likelihood maps for three periods in 2018. A quantitative summary is provided in Table 2 for both flood events. The overpasses that occur at the maximum flood extent yield the largest percentage of high (i.e., >90% inundation likelihood) likelihood values around 16% for both events (Figure 5b). Conversely, overpasses at the end of the flood cycle indicate an increase in modeling uncertainty, with fewer high likelihood cells (~5% for both events) and more cells in the lowest (10%–30% inundation likelihood) category (3.2% and 4.0% for 2009 and 2018, respectively). Comparing Figure 5b with Figure 5c, the regions with likelihood values over 70% are small, with no clear pattern of consistently flooded sections of the floodplain. The January 2018 (Figure 5a) overpass has similar proportions of higher and lower likelihood cells (Table 2) but with more distinct regions of high likelihood values.

Larger differences in model performance between the 2 years are observed for the NSE values than for the F^2 statistics (Figure 4). For the 2009 event, NSE values from all simulations are relatively high (0.74–0.82), with an

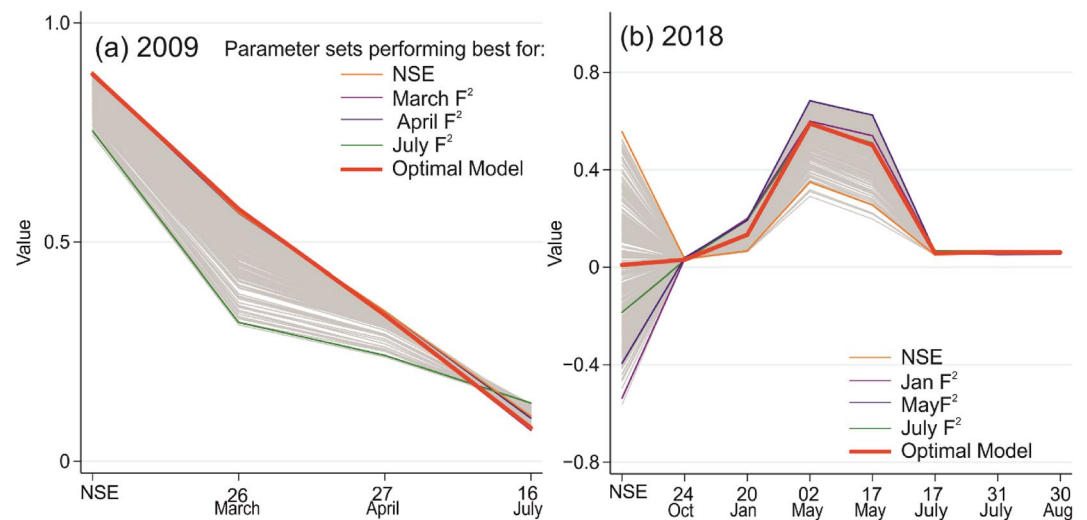


Figure 4. Analysis of model performance across the complete emulator training set for each metric for (a) 2009 and (b) 2018. Each gray line represents a model run. The y axis plots *NSE* for the left-most point and F^2 for the dates of each LandSAT scene. The best fitting model parameters for each validation point (*NSE* overall and F^2 for each LandSAT scene) are selected and the model performance for each is evaluated at all other validation points as indicated by the colored lines. The overall best performing parameter set is also highlighted.

average value of 0.79. By contrast the maximum value for the more complex doubled-peaked hydrograph of 2018 (0.51) is lower than for any model in 2009 with a wider range of results.

The benefit of the multiobjective model calibration/validation is demonstrated in Figure 4, where the optimum simulation for individual calibration points is highlighted. It shows that parameters that score well for March or the *NSE* do not necessarily score well for other points. For example, the optimum model for the July overpass (green line) produces one of the lowest March F^2 values. A similar parameter set produces the highest F^2 value for July 2018, characterized by a higher channel depth (5.2 m for 2009 and 5.4 m for 2018), similar evaporation rates (16% above the calculated average value for both simulations), and similar channel friction values (0.023 for 2009, 0.016 for 2018) and floodplain friction values (0.044 for 2009 and 0.046 for 2018). For the 2018 model, the wider variety in the evaluation of *NSE* creates a more refined model selection by removing a significant number of simulations that appear acceptable based on F^2 values. Simulations that perform well in modeling the inundation extents in May and June (blue and green lines) result in negative *NSE* values. Similarly, the model with the highest *NSE* value, produces some of the lowest F^2 values for May and July.

The final optimal parameter set was based on the best result for all 400 calibration simulations for 2009 event. The same parameter set when validated on the 2018 data produced a peak F^2 value of 0.61 with a peak *NSE* score of 0.45. Comparing across all the 400 simulations for the 2018 event, it can be seen that similar parameter values produced the optimum result as the 2009 set, with floodplain friction values (0.49 and 0.48), and channel bed depth values (4.4 and 4.3 m) for 2009 and 2018, respectively. The channel depth value was equal to the average value recorded in the bathymetry data. There are more significant differences in the value for the channel Manning's n value (0.21 and 0.13). Considering the relatively low values achieved for the other phases in the modeled events, the parameters for the final calibrated model was selected based on producing the best score between F^2 for the peak of the 2009 event and the *NSE* value (as determined by the position of the model and the pareto front), and producing an acceptable score for the peak of the 2018 event and *NSE* for the 2018 event ($F^2 > 0.5$, $NSE > 0.3$).

4.2. Sensitivity Analysis

The sensitivity analysis results are summarized in Table 3. For the 2009 event, the floodplain friction parameter accounts for over 95% of the variation in results for the Nash Sutcliffe, and the April and March overpasses. For the July overpass, the channel depth also accounts for part of the variance. Infiltration and evaporation have little contribution to model variance at any time of year, including the July overpass evaluation. The influence of the

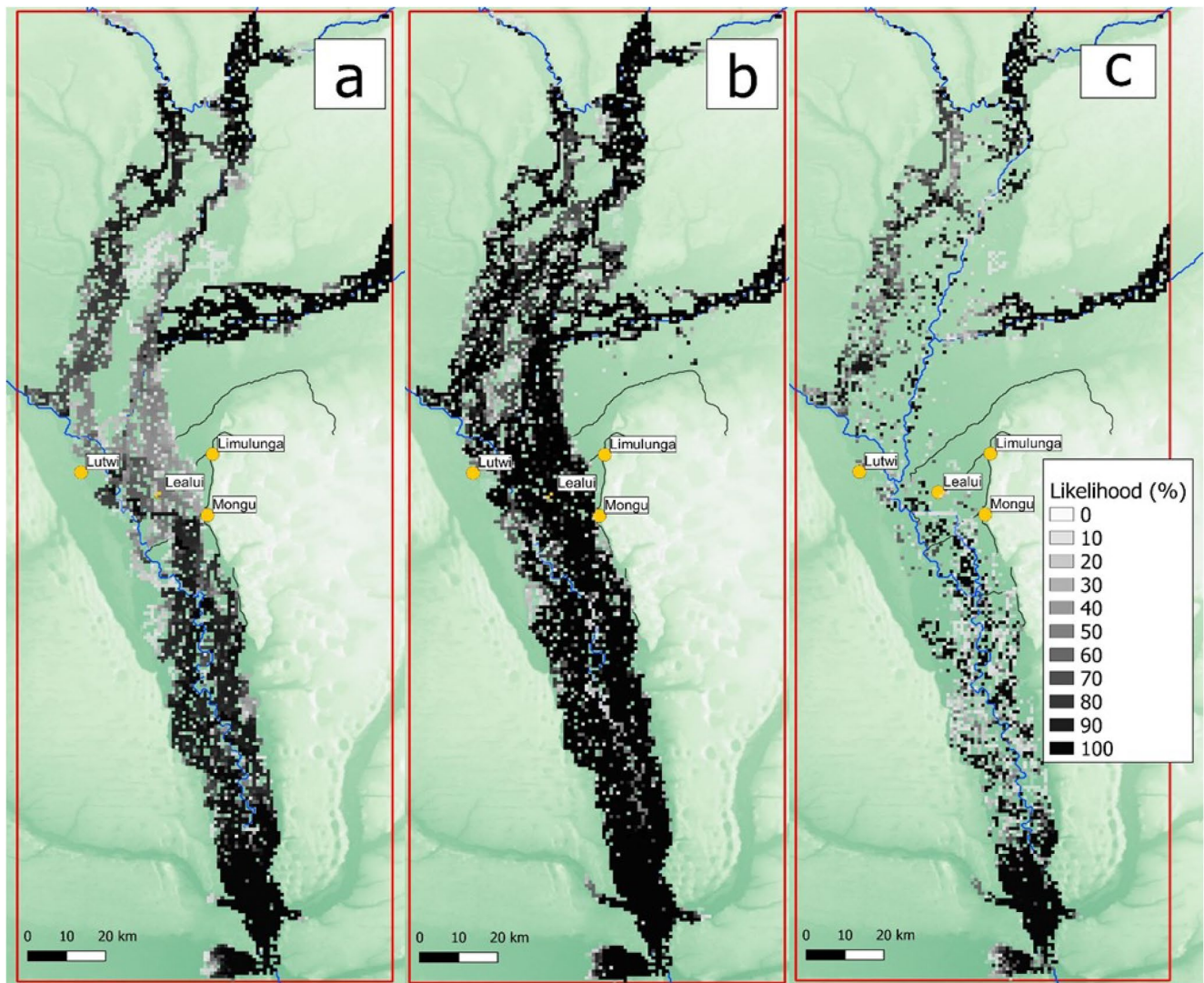


Figure 5. Likelihood plots for the 2018 model calibration for (a) 24 January, (b) 2 May, and (c) 17 July. Each cell presents the percentage of model simulations where the cell is inundated across the calibration and sensitivity analysis training models.

parameters is visualized in Figure 6, which provides a visual comparison of model results for the March 2009 flood extent (Figure 6 top) against changing values of all input parameters.

By comparison, the results from the 2018 event show that the channel friction (60%–70%) and channel depth (28%–42%) parameters have a greater influence on model results. Floodplain friction has now reduced as a significant parameter, with contribution to variation being around 3%–9%. As with the 2009 results, the 2018 results are consistent across all the model evaluations; however, for the final July inundation extent, there are multiple parameters which have a significant contribution to variance in the model results. In comparison to the top half of Figure 6, the clear dominance of one parameter is replaced with broader distribution of model results across the range of parameter values. Contributions to variance from infiltration (30%), channel depth (42%), and channel friction (20%), can all be considered high, and as with 2009 events, the value of evaporation has low significance on model results. Higher order influences were not significant in comparison to the primary effect of each parameter.

Table 2
Consensus of Simulations on Cell Inundation Status

Inundation frequency	0	10%–30% (Low)	30%–60%	60%–90%	90%–100% (High)
Time Slice	2009 Event				
March 2009	76.1	1.7	3.1	2.3	16.8
April 2009	83.6	1.2	1.8	2	11.5
July 2009	90	3.1	1.1	0.3	5.3
Time Slice	2018 Event				
January 2018	80.8	3.6	3.4	2.3	9.9
2 May 2018	78.2	2.4	1.4	2.2	15.9
17 May 2018	79.2	3.1	1.8	3.2	12.7
July 2018	87.8	4	1.8	1.3	5.1

Note. Summary cell values from the likelihood analysis expressed as a percentage of the whole model domain.

4.3. High Resolution Hydraulic Model

Running LISFLOOD-FP at 100 m spatial resolution yielded similar results to the model calibration and validation with the best model performance observed during the flood peaks (F^2 scores of 0.56 and 0.62 for 2009 and 2018, respectively), and lower performance for the recession and rise phase of the flood (0.13 and 0.10 for July 2009 and 2018, respectively). The NSE values were 0.93 and 0.80 for 2009 and 2018. This confirms the assumption that the model could be calibrated and validated at the lower resolution with parameters established during that process being applied to a higher resolution model. Again, we emphasize that this assumption is valid in this model application as it is appropriate given the dominant hydrodynamic processes and underlying topography. The assumption is not applicable as a general approach to hydrodynamic model development. In this case, the calibration values are acceptable, rather than optimal. Figure 7a provides a visual comparison of the model results against LandSAT NDWI classified water bodies for the peak of the 2018 flood.

Regions of apparent model over prediction occur close to the river; however, ground-truthing revealed the presence of partially submerged long grasses at these locations. Such vegetated water can be challenging to identify as inundated using the LandSAT NDWI method (Hardy et al., 2019). Under prediction is limited to the northern extent of the model, where the Lungwebungu River discharges into the floodplain and the Luena valley.

In comparison to the Senanga gauge data, both models display a similar peak discharge to the observed data (Figure 8). For the 2009 event, the model underestimates the observed peak by 1.7%, with a 6-day delay in comparison to the observed event. The 2018 model overestimates the peak of event by 12% predicting the peak time 2 days earlier than observed. The 2 years of the model match the observed rising limb differently. For the 2018 simulation, the model produces a consistently higher discharge (5%–10%) for the majority of the rising limb, whereas the 2009 simulation matches observed values more closely. This overestimation is offset slightly by the more dramatic recession flow which is also observed in the 2009 model.

4.4. Floodplain Dynamics

Using the high-resolution model, the dynamics of flooding within the valley can be identified. Initial overtopping of channel banks is observed near to the convergence of the Zambezi and the Luanginga River, with the flood wave traveling south and north from this location, until the time of peak discharge. This pattern is confirmed via analysis of the LandSAT imagery. The floodwaters in the Barotse have significant control on the Lungwebungu valley, by creating a backwater effect, which impacts flooding along this valley. At peak discharge, the entire floodplain is inundated after which the coherence of the flood waters as a single expanse of water reduces as the gradual draining and water losses isolates flood waters. The Luena valley also remains inundated throughout

Table 3
Sensitivity Analysis Results for the 2009 and 2018 Event Showing the Percentage of Influence of Each Parameter on the Model Variability for Each Metric Used in the Calibration Phase

Parameter	NSE 2009	F^2 March 2009	F^2 April 2009	F^2 July 2009	NSE 2018	F^2 January 2018	F^2 2nd May 2018	F^2 17th May 2018	F^2 July 2018
Floodplain n	95.0	93.1	90	75.1	3.1	0.3	9.3	7.1	4.1
Channel n	0.0	0.0	0.0	1.3	73.1	74.6	61.1	65.1	20.4
Infiltration (mm hr ⁻¹)	1.1	0.3	2.5	6.1	0.01	0.2	0.50	0.4	30.4
Evaporation (mm d ⁻¹)	0.1	0.2	2.3	0.4	0.03	0.3	0.3	0.3	1.2
Channel Depth (m)	4.2	6.5	5.2	19.4	23.9	24.6	28.3	26.9	42.2
Initial depth (m)	0.1	0.2	2.8	0.3	0.04	0.0	0.38	0.26	1.52

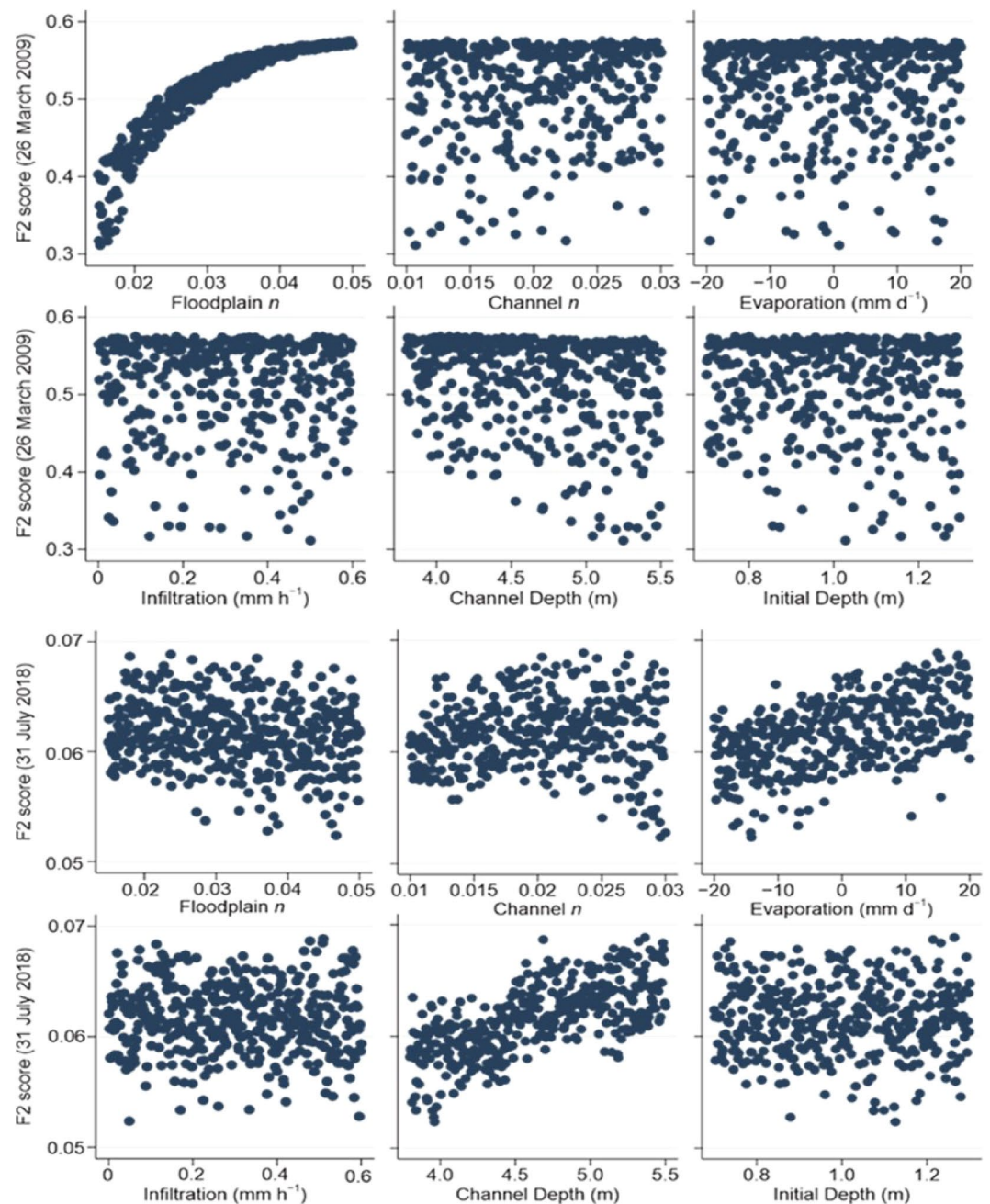


Figure 6. Dotty plot comparison of each set of input parameters against the inundation extent model evaluation function for the March 2009 overpass (top) and July 2018 overpass (below). Each dot, taken from the emulator training, represents a single model simulation.

this time, although the water depths reduce considerably from July until September. Aside from the timing of the peaks in the separate years, the maximum extent of flooding and the patterns of inundation are similar.

The impact of the floodplain modifications is more noticeable in the recession phase of events, which can be seen in the analysis of the July overpasses. The 2009 model predicts more extensive volumes of flood water in the southern part of the floodplain, compared to the 2018 event. In both model and LandSAT classifications, there are wider extents of flood water and water bodies on the floodplain in 2009, despite the earlier peak discharge.

To clarify the effects of the canal modification and causeway construction, each flood event was run on the opposite terrain data set (the “cross-comparison models” of Figure 8). Adding in the floodplain modifications to the

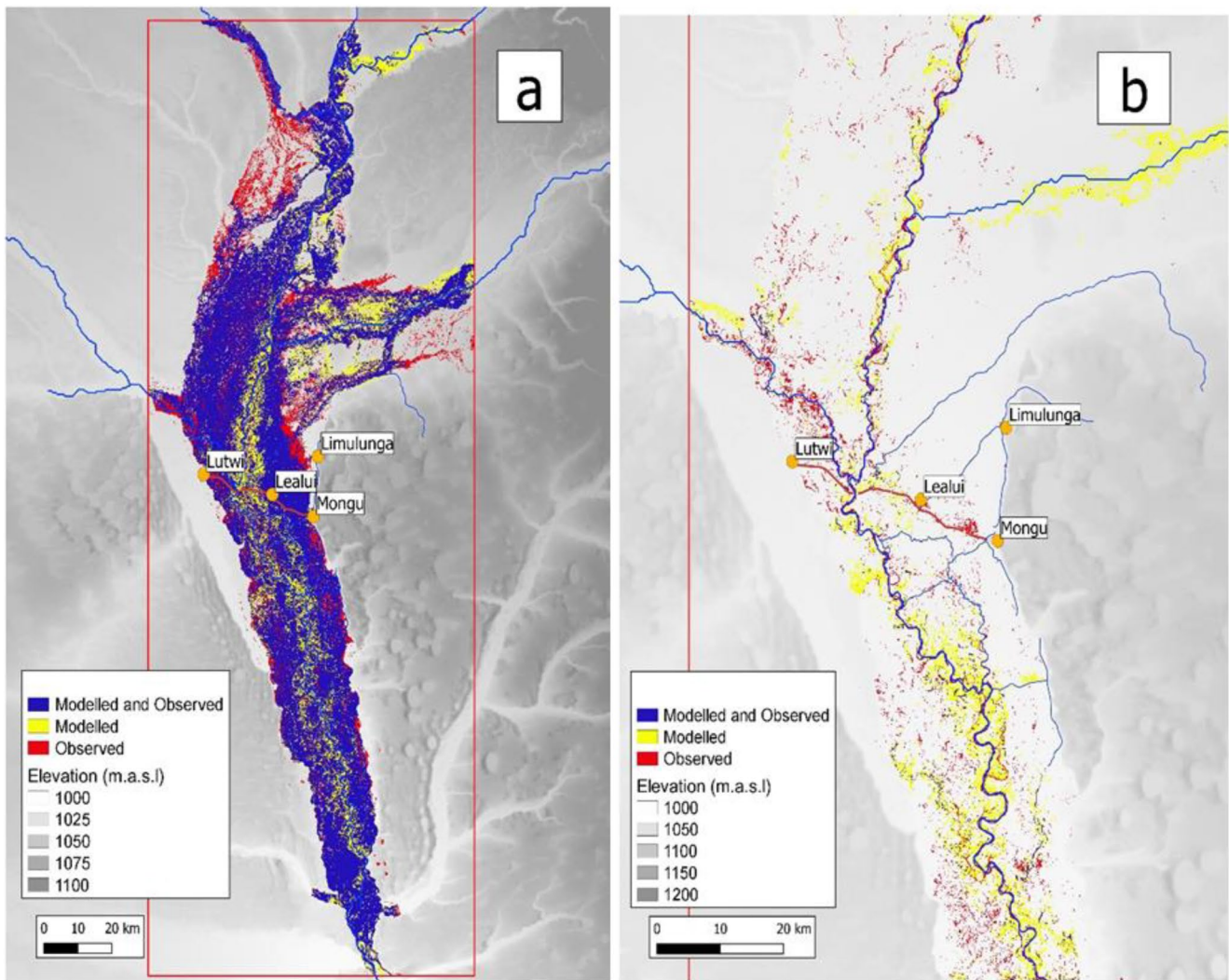


Figure 7. Comparison of the modeled output with LandsAT imagery for (a) May 2018 and (b) July 2018.

simulated 2009 event lead to a 5% increase in the flood peak. Conversely, removing them from the 2018 event yielded a 10% lower peak (Figure 8a). Although peak flow inundation extents are similar, there is a more noticeable difference in timing of the drawdown. The area of flooding increases by 9% for the 2018 event run on the 2009 DTM (i.e., without the canals built in 2014), whilst the 2009 event reduces by 24% on the 2018 DTM (with canals) at the beginning of July in the simulation. The changes in flooding patterns and depths are not spatially uniform. At the flood peak, the canals and causeway change the pattern of water depths (Figure 8b). Regions with deeper waters (represented by the red areas) as a result of the modifications are prevalent on the west side of the floodplain and north from the causeway, which has reduced the conveyance of the floodplain. The eastern side of the floodplain has shallower depths at peak discharge (represented by the blue regions), due to the two restored canals increasing drainage of this region. South of the causeway around Mongu, the modifications reduce the levels of water on the eastern bank but increase the depths of water along the western bank, as a result of the increased drainage of the canals.

The modifications of the floodplain have further impacted the timing and duration of inundation, which in turn will impact accessibility of the local population to health facilities, and the length of time of environmental suitability for the malaria vector. The difference in the length of time each cell is classified as accessible is presented in Figure 8c, where access is defined as water being no more than 0.3 m deep, an approximate depth for vehicles to travel through. For 55% of cells on the floodplain accessibility time is reduced, represented by the blue regions of Figure 8c. For regions around Mongu (Figure 8c) access has increased in the region of 9–12 weeks, as a result

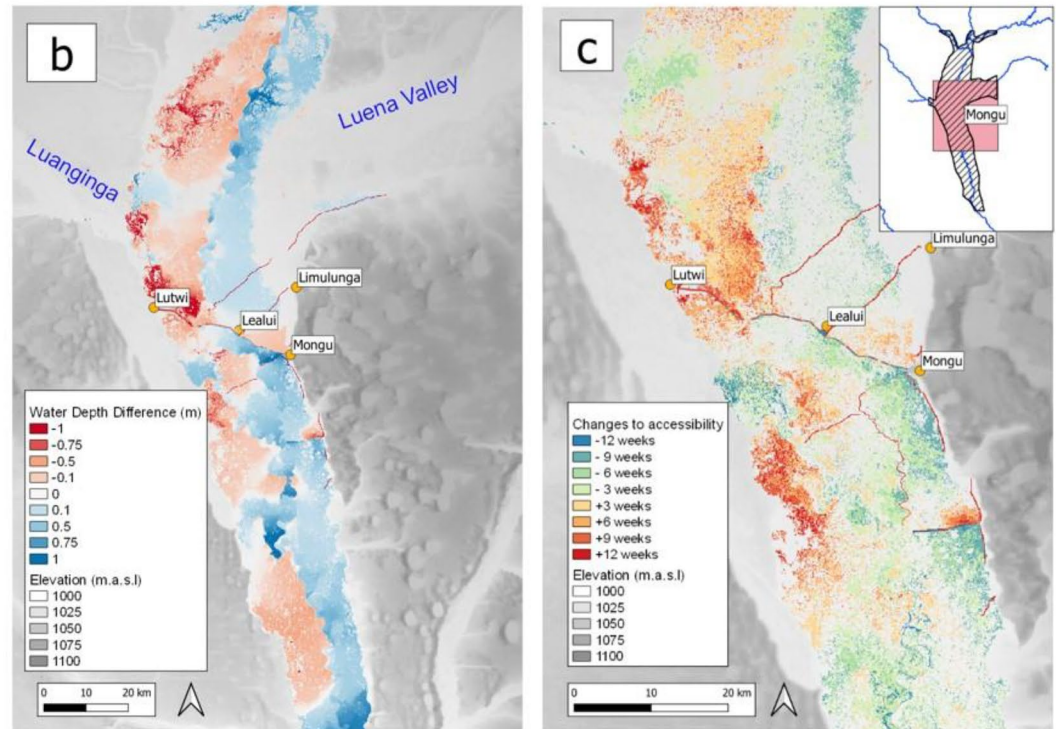
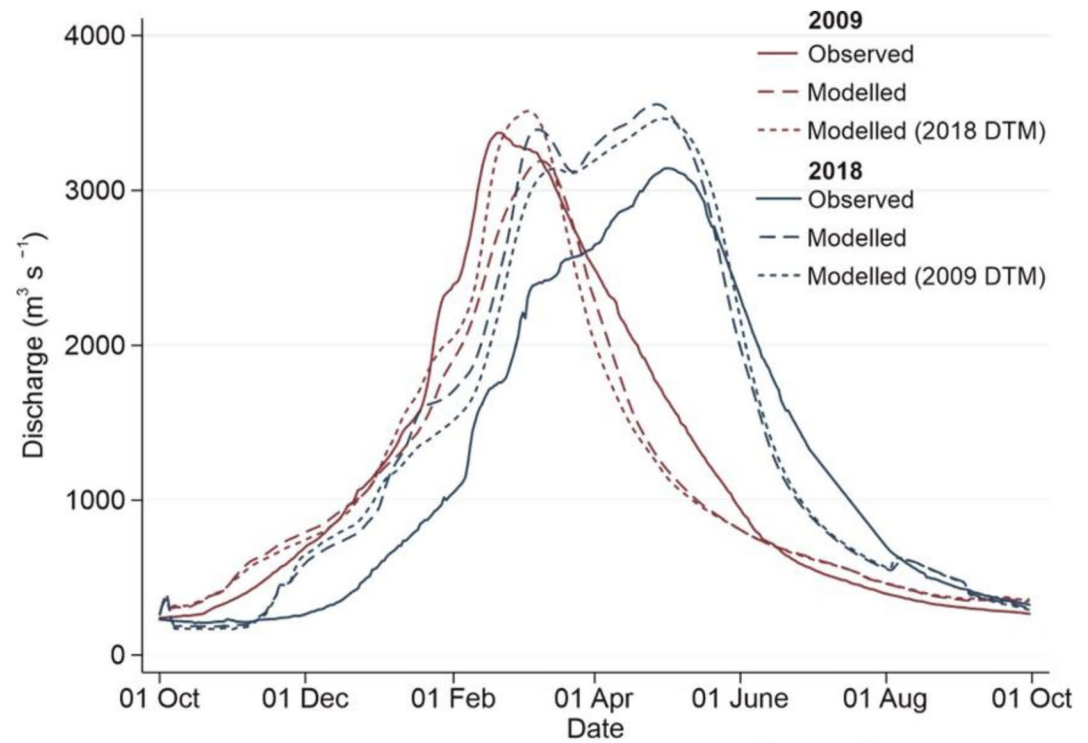


Figure 8. (a) Comparison of observed data at the Senanga flow gauge (solid lines) against the high-resolution models (long dash) and “cross-comparison model” (short dash) for 2009 (red) and 2018 (blue). The maps below (b, c) present the difference in model output between the 2009 event run on the 2018 and 2009 DTM. (b) Comparison of water depths during the March overpass. Red regions are areas of deeper water on the 2018 DTM model, and blue regions for the 2009 DTM model. (c) Focused view of changes to access through the floodplain as a result of the modifications to the floodplain. Negative values are increasing lengths of time inundated on the 2018 DTM.

of the early draw down of the canals, and the reduced flood peak depths seen in Figure 8b. The west of the floodplain has longer inaccessible periods, whilst the east has shorter inaccessible periods.

5. Discussion

The development of the Barotse floodplain hydrodynamic model has highlighted several important aspects of modeling a complete flood cycle and changes to the hydrodynamics of the floodplain arising from infrastructure modifications.

5.1. Floodplain Modifications

In terms of understanding the floodplain hydrodynamic processes, a key finding of this research is that the floodplain modifications have increased the rate at which the floodplain drains and increased the influence of the drainage network on the overall floodplain hydraulics. The extent of the reduction in inundation is notable, with a 24% reduction in the inundated area during the recession limb when the 2009 flood event was simulated with the improved waterways added. While the overall impact of the canal network is an increase in the flow rate through the floodplain, the effect is not spatially uniform. The combination of the causeway and the canals has altered the dynamics of the flooding cycle, first by restricting flow at the location of initial overtopping, and second by transferring water through the canal network to the eastern side of the floodplain. Previous studies using hydrological and 1D channel models have identified the impact of modifications to the channel parameters on both peak discharge and flood extent values (e.g., Fleischmann et al., 2018; Liu et al., 2018). This effect is also reflected in the results of the sensitivity analysis (Table 3). The floodplain friction parameter is the most significant parameter for most evaluation points in the 2009 event, but channel friction becomes more important for the 2018 event. This difference highlights how the floodplain represents an extended channel during peak flood conditions, with the channel having little influence on the outputs at this stage. The channels had an effect even at peak flow conditions, despite the relatively small-scale changes to the channel network. The low influence of channel conveyance for the 2009 event, represented by the low sensitivity analysis scores for channel depth and friction, further highlights the influence of the modifications on overall flood dynamics. A caveat to this is that the 1D network used here is based on a simplified diffusion wave-based approach and also does not allow explicit representation between linked channels, unlike the subgrid approach which had also been tested. For this study, these issues were less significant than other sources of uncertainty but this may not be true in other catchments and test cases. In order to understand this further, future research should investigate using more complex numerical models for the channel network than has been used here.

Finally, it should be noted that these results are based on two above average flood events, and may not be representative of typical years that influence access to health facilities. As only two events of similar magnitude have been used in this analysis, further work with events of varying magnitude will be required to determine the impact on health facility access further, a more refined approach to healthcare access would be required to understand the implications of these results from an operations perspective.

5.2. Model Performance

The hydrodynamic model performance was highest at peak discharge, whilst the lowest F^2 results occur during the recession phase of flooding. The numeric model is optimized for replicating flood peaks; further work is required to produce more holistic models capable of replicating the complete flood cycle. Poorer model performance during periods of low flow has been previously identified by several authors (Fernandez et al., 2016; Paiva et al., 2011; Pinel et al., 2020; Rudorff et al., 2014; Tan et al., 2019; Yamazaki et al., 2012). The low model performance values can be seen indirectly in Figure 5c and Table 2 which shows a similar range of values in both the rise (January) and recession (July) of the flood. The underlying cause for this could include the impact of microtopographical features not sufficiently represented at the 100 m grid resolution, the issues of classifying smaller water body features and the ability to model losses and changes to microwater body features at the floodplain scale.

A potential cause of this poorer performance is the classification of water bodies. In this study, the standard NDWI index is used, but alternative methods, such as a modified NDWI method (Xu, 2005) were also tested.

These alternative methods tend to overestimate water body formation in the rise and recession phases of the model (Pan et al., 2020). Conversely, our use of NDWI has resulted in an observation set with fewer water bodies in the recession phase as it is incapable of detecting vegetated water bodies as confirmed by ground surveys (see Hardy et al., 2019). The result is an observation set that over penalizes simulations with a wider flood extent. Furthermore, the water bodies become shallow, more disparate, and less coherent in size and shape, compared to the initial phase of flooding characterized by fewer water bodies that increase in size over time. The complexity of identifying these water bodies across a floodplain is observed elsewhere (Tan et al., 2019) and highlights that methods and data sets that can improve identification of these features is key to future model development.

Uncertainty in terrain data presents a further issue relating to accurate determination of water body formation in the recession phase of the flooding. TanDEM-X1 data can contain large errors related to backscatter and requires preprocessing before use in a flood model (Archer et al., 2018). In this study, the relative simplicity of the floodplain has reduced the impact that variable vegetation cover may have on the DTM, and therefore the model results. Yet, uncertainty in topographic data may still influence the location of water bodies created in the recession of the flood waters. Additional research incorporating terrain uncertainty, in particular any potential issues surrounding either resampling methods or errors inherent in the data sets, is required to understand the impact of these on receding flood waters. Such further analysis will be critical in producing accurate representations of water body locations in other studies and environments.

5.3. Model Calibration and Validation Approaches

The complexity of modeling flood recessions is further demonstrated by the lack of a single influential parameter in the sensitivity analysis for the July 2018 overpass. A single influential parameter demonstrates that an underlying process dictates model output (such as Floodplain Manning's n value for the 2009 event). Based on this, an area for model development is to improve the simple approaches to water loss mechanisms in the model presented here, and to represent some of the dynamic components of these processes (e.g., Fernandez et al., 2016; Fleischmann et al., 2018).

The issue of modeling flood recessions highlights the importance of using multiple functions for model calibration. By using multiple data sets, including the conventional outflow hydrograph NSE value, issues with overfitting the model to a particular moment in time or data set are mediated (e.g., Dung et al., 2011). The potential for such overfitting is evident in Figure 4, where the maximum performing parameter sets for dry season inundation extents result in poorer NSE fits for 2018, requiring compromise between the data sets for a satisfactory model to be created.

5.4. Implications

The implication of this study is that floodplain hydrodynamics are sensitive to changes in both floodplain and channel characteristics. There is potential for river network changes to have a substantial effect on floodplain dynamics (see also the findings of Shastry et al. (2020) for the Lagone floodplain in Cameroon). Critically, the increased drawdown promoted by the restored waterways reduces the number of surface water bodies during the recession of the flood wave. Such hydrological changes can have important consequences for malaria transmission, altering the spatial and temporal variability of potential water body habitats and also the nature of those habitats (Hardy et al., 2013; Smith et al., 2013). The variations of the water levels as a result of the modifications to the floodplain will also impact access to villages and health facilities. For health facilities on the west bank of the river, changes to the peaks will require careful analysis to ensure the correct supplies are provided prior to the onset of flooding.

6. Conclusion

An ability to model fluvial inundation dynamics over large African floodplains is of critical importance across the continent. Seasonal flooding both alters and disrupts access networks linking settlements to health centers and other key infrastructure. While many floodplain communities are well adapted to the seasonal flooding inherent in such systems, the annual variability in flood extents can be disruptive in both high and low flow years. To

date, the size of such systems (with typical dimensions of over 100 km²) has precluded detailed hydrodynamic modeling.

The development of the hydrodynamic model has revealed key hydrodynamic processes and demonstrated the complexity of developing a model that can fit multiple objectives and time points within the calibration period, in particular the rise and recession phases of flooding. Further modeling of similar systems will be required to understand the general application of this approach and hydrodynamic models to these environments.

The development and application of a hydrodynamic model to the Barotse floodplain in Zambia has revealed a key hydrodynamic process in the annual flood cycle: the importance of the floodplain in the conveyance of waters through the floodplain. A notable shift occurs in the relative importance of in-channel and floodplain flows in determining flood characteristics between the 2009 and 2018 annual floods. This shift corresponded to improvement to a floodplain canal network in 2014. The canals increased the rate of flood water drawdown following the annual flood and reduced flood extents during the recession limb, while also increasing peak flood discharges. The implication is that further modifications to the floodplain should be carefully considered due to implications to ecosystems services.

Conflict of Interest

The authors declare no conflicts of interest relevant to this study.

Data Availability Statement

The data that support the findings of this study are available from the authors, including the model boundary conditions, river cross section data and calibration data sets from the following repository doi:10.6084/m9.figshare.20209799 (Figure Data) The LandsAT imagery use to calibrate and validate the model can be downloaded from the open access earthexplorer.usgs.gov/ web portal (Earth Explorer LandsAT data). This requires an account to be setup to access the data. The data used was the LandsAT 5, 7 and LandsAT 8 data collections, from the dates indicated in Figure 2 and using path and row number 175070 and 175071. The data can be downloaded through the portal, or via the bulk download system. The **TanDEM Data** are available at <https://tandemx-science.dlr.de/> A registered user access is required to access the data and to submit data requests. The basic product 12 and 30 m global TanDEM-X DEMs (used in this study) can be ordered by users via a proposal submission, the full process of which is available here—<https://tandemx-science.dlr.de/cgi-bin/wcm.pl?page=TDM-Proposal-Submission-Procedure> (TanDEM Data). After a successful evaluation of the submitted proposal, the requested data will be made via an FTP website in geotiff format. A license agreement is required to access this data—<https://tandemx-science.dlr.de/pdfs/TSX-TDX-user-license-v2.2.pdf>. The Bayesian Calibration of Computer Code (BACCO) version 1.2. used in the sensitivity analysis is available as an R package from the open source cran repository; <https://CRAN.R-project.org/package=BACCO> (BACCO Software). No account is required, and is available under a GNU General Public License v3.0. The hydraulic model used in this study is the LISFLOOD-FP version 8.1 The source code of LISFLOOD-FP8.0 is available under a GNU General Public License v3.0 for any noncommercial use and can be downloaded at <https://doi.org/10.5281/zenodo.4073011> (LISFLOOD Software). The river gauge data were obtained from www.warma.org.zm/warma-about-us/contact (River Gauge data).

Acknowledgments

We thank the people of Barotseland for their warm welcome and guidance, and our colleagues in the University of Barotseland. We are especially grateful to Vincent Siazuyu, Limulunga District Environmental Health Officer and colleagues in the Zambezi EcoHealth Partnership and programme manager Alex Malloy. This work is funded by the UK Natural Environment Research Council (Grant Ref: NE/P013481/1). We also thank the two anonymous reviewers for their helpful comments and insights, and to Jeff Neal for his comments, help and guidance in using LISFLOOD-FP correctly.

References

- Alfieri, L., Bisselink, B., Dottori, F., Naumann, G., de Roo, A., Salamon, P., et al. (2017). Global projections of river flood risk in a warmer world. *Earth's Future*, 5, 171–182. <https://doi.org/10.1002/2016EF000485>
- Archer, L., Neal, J. C., Bates, P. D., & House, J. I. (2018). Comparing TanDEM-X data with frequently used DEMs for flood inundation modeling. *Water Resources Research*, 54, 10205–10222. <https://doi.org/10.1029/2018WR023688>
- Arnold, J. G., Srinivasan, R., Muttiyah, R. S., & Williams, J. R. (1998). Large area hydrologic modeling and assessment. Part I: Model development. *Journal of the American Water Resources Association*, 34(1), 73–89. <https://doi.org/10.1111/j.1752-1688.1998.tb05961.x>
- Aronica, G., Bates, P. D., & Horritt, M. S. (2002). Assessing the uncertainty in distributed model predictions using observed binary pattern information within GLUE. *Hydrological Processes*, 16(10), 2001–2016. <https://doi.org/10.1002/hyp.398>
- BACCO Software. Retrieved from <https://CRAN.R-project.org/package=BACCO>
- Bates, P. D., & De Roo, A. P. J. (2000). A simple raster-based model for flood inundation simulation. *Journal of Hydrology*, 236(1–2), 54–77. [https://doi.org/10.1016/S0022-1694\(00\)00278-X](https://doi.org/10.1016/S0022-1694(00)00278-X)

- Bates, P. D., Horritt, M. S., & Fewtrell, T. J. (2010). A simple inertial formulation of the shallow water equations for efficient two-dimensional flood inundation modelling. *Journal of Hydrology*, 387(1–2), 33–45. <https://doi.org/10.1016/j.jhydrol.2010.03.027>
- Bernhofen, M. V., Whyman, C., Trigg, M. A., Sleigh, P. A., Smith, A. M., Sampson, C. C., et al. (2018). A first collective validation of global fluvial flood models for major floods in Nigeria and Mozambique. *Environmental Research Letters*, 13, 104007. <https://doi.org/10.1088/1748-9326/aae014>
- Beven, K. (2007). Towards integrated environmental models of everywhere: Uncertainty, data and modelling as a learning process. *Hydrology and Earth System Sciences*, 11(1), 460–467. <https://doi.org/10.5194/hess-11-460-2007>
- BRLi and NIRAS. (2014). Detailed assessment, conceptual design and Environmental and Social Impact Assessment (ESIA) study for the improved use of priority traditional canals in the Barotse sub-basin of the Zambezi.
- Cai, X. L., Haile, A. T., Magidi, J., Mapedza, E., & Nhamo, L. (2017). Living with floods—Household perception and satellite observations in the Barotse floodplain, Zambia. *Physics and Chemistry of the Earth*, 100, 278–286. <https://doi.org/10.1016/j.pce.2016.10.011>
- Chikozho, C., & Mapedza, E. (2017). In search of socio-ecological resilience and adaptive capacity: Articulating the governance imperatives for improved canal management on the Barotse floodplain, Zambia. *International Journal of the Commons*, 11(1), 119–143. <https://doi.org/10.18352/ijc.636>
- Chow, V. T., Maidment, D. R., & Mays, L. W. (1988). *Applied hydrology*. McGraw Hill Book Company.
- Cohen Liechti, T., Matos, J. P., Boillat, J. L., Portela, M. M., & Schleiss, A. J. (2014). Hydraulic-hydrologic model for water resources management of the Zambezi basin. *Journal of Applied Water Engineering and Research*, 2(2), 105–117. <https://doi.org/10.1080/23249676.2014.958581>
- Coughlan de Perez, E., Stephens, E., Bischiniotis, K., van Aalst, M., van den Hurk, B., Mason, S., et al. (2017). Should seasonal rainfall forecasts be used for flood preparedness? *Hydrology and Earth System Sciences*, 21(9), 4517–4524. <https://doi.org/10.5194/hess-21-4517-2017>
- Dung, N. V., Merz, B., Bárdossy, A., Thang, T. D., & Apel, H. (2011). Multi-objective automatic calibration of hydrodynamic models utilizing inundation maps and gauge data. *Hydrology and Earth System Sciences*, 15, 1339–1354. <https://doi.org/10.5194/hess-15-1339-2011>
- Dunne, T., & Aalto, R. E. (2013). 9.32 large river floodplains. In J. F. Shroder (Ed.), *Treatise on geomorphology* (pp. 645–678). Academic Press. <https://doi.org/10.1016/b978-0-12-374739-6.00258-x>
- Earth Explorer LandSAT data. Retrieved from <https://earthexplorer.usgs.gov/>
- Faruk, N., Surajudeen-Bakinde, N. T., Abdulkarim, A., Oloyede, A. A., Olowoyin, L., Bello, O. W., et al. (2020). Rural healthcare delivery in sub-Saharan Africa: An ICT-driven approach. *International Journal of Healthcare Information Systems and Informatics*, 15(3), 1–21. <https://doi.org/10.4018/ijhisi.2020070101>
- Fernandez, A., Najafi, M. R., Durand, M., Mark, B. G., Moritz, M., Jung, H. C., et al. (2016). Testing the skill of numerical hydraulic modeling to simulate spatiotemporal flooding patterns in the Logone floodplain, Cameroon. *Journal of Hydrology*, 539, 265–280. <https://doi.org/10.1016/j.jhydrol.2016.05.026>
- Ficchi, A., & Stephens, L. (2019). Climate variability alters flood timing across Africa. *Geophysical Research Letters*, 46, 8809–8819. <https://doi.org/10.1029/2019GL081988>
- Fick, S. E., & Hijmans, R. J. (2017). WorldClim 2: New 1-km spatial resolution climate surfaces for global land areas. *International Journal of Climatology*, 37(12), 4302–4315. [10.1002/joc.5086](https://doi.org/10.1002/joc.5086)
- Fleischmann, A., Siqueira, V., Paris, A., Collischonn, W., Paiva, R., Pontes, P., et al. (2018). Modelling hydrologic and hydrodynamic processes in basins with large semi-arid wetlands. *Journal of Hydrology*, 561, 943–959. <https://doi.org/10.1016/j.jhydrol.2018.04.041>
- Grimaldi, S., Petroselli, A., Arcangeletti, E., & Nardi, F. (2013). Flood mapping in ungauged basins using fully continuous hydrologic–hydraulic modeling. *Journal of Hydrology*, 487, 39–47. <https://doi.org/10.1016/j.jhydrol.2013.02.023>
- Grimaldi, S., Schumann, G. J. P., Shokri, A., Walker, J. P., & Pauwels, V. R. N. (2019). Challenges, opportunities, and pitfalls for global coupled hydrologic–hydraulic modeling of floods. *Water Resources Research*, 55, 5277–5300. <https://doi.org/10.1029/2018WR024289>
- Hall, J. W., Boyce, S. A., Wang, Y. L., Dawson, R. J., Tarantola, S., & Saltelli, A. (2009). Sensitivity analysis for hydraulic models. *Journal of Hydraulic Engineering-ASCE*, 135(11), 959–969. [https://doi.org/10.1061/\(asce\)hy.1943-7900.0000098](https://doi.org/10.1061/(asce)hy.1943-7900.0000098)
- Hall, J. W., Manning, L. J., & Hankin, R. K. S. (2011). Bayesian calibration of a flood inundation model using spatial data. *Water Resources Research*, 47, W05529. <https://doi.org/10.1029/2009WR008541>
- Hardy, A., Ettrich, G., Cross, D. E., Bunting, P., Liywali, F., Sakala, J., et al. (2019). Automatic detection of open and vegetated water bodies using Sentinel 1 to map African malaria vector mosquito breeding habitats. *Remote Sensing*, 11(5), 593. <https://doi.org/10.3390/rs11050593>
- Hardy, A. J., Gamarra, J. G., Cross, D. E., Macklin, M. G., Smith, M. W., Kihonda, J., et al. (2013). Habitat hydrology and geomorphology control the distribution of malaria vector larvae in rural Africa. *PLoS One*, 8(12), e81931. <https://doi.org/10.1371/journal.pone.0081931>
- IWMI. (2014). *Wetlands and people*. International Water Management Institute (IWMI).
- Kling, H., Stanzel, P., & Preishuber, M. (2014). Impact modelling of water resources development and climate scenarios on Zambezi River discharge. *Journal of Hydrology: Regional Studies*, 1, 17–43. <https://doi.org/10.1016/j.ejrh.2014.05.002>
- Komi, K., Neal, J., Trigg, M. A., & Diekkrüger, B. (2017). Modelling of flood hazard extent in data sparse areas: A case study of the Oti River basin, west Africa. *Journal of Hydrology: Regional Studies*, 10, 122–132. <https://doi.org/10.1016/j.ejrh.2017.03.001>
- Leauthaud, C., Duvail, S., Hamerlynck, O., Paul, J. L., Cochet, H., Nyunja, J., et al. (2013). Floods and livelihoods: The impact of changing water resources on wetland agro-ecological production systems in the Tana River Delta, Kenya. *Global Environmental Change-Human and Policy Dimensions*, 23(1), 252–263. <https://doi.org/10.1016/j.gloenvcha.2012.09.003>
- Lewin, J., & Ashworth, P. J. (2014). The negative relief of large river floodplains. *Earth-Science Reviews*, 129, 1–23. <https://doi.org/10.1016/j.earscirev.2013.10.014>
- Lindström, G., Johansson, B., Persson, M., Gardelin, M., & Bergström, S. (1997). Development and test of the distributed HBV-96 hydrological model. *Journal of Hydrology*, 201, 272–288.
- LISFLOOD Software. <https://doi.org/10.5281/zenodo.4073011>
- Liu, Z., Merwade, V., & Jafarzadegan, K. (2018). Investigating the role of model structure and surface roughness in generating flood inundation extents using one- and two dimensional hydraulic models. *Journal of Flood Risk Management*, 12, e12347. <https://doi.org/10.1111/jfr3.12347>
- Michailovsky, C. I., & Bauer-Gottwein, P. (2014). Operational reservoir inflow forecasting with radar altimetry: The Zambezi case study. *Hydrology and Earth System Sciences*, 18(3), 997–1007. <https://doi.org/10.5194/hess-18-997-2014>
- Neal, J., Schumann, G., & Bates, P. (2012). A subgrid channel model for simulating river hydraulics and floodplain inundation over large and data sparse areas. *Water Resources Research*, 48, W11506. <https://doi.org/10.1029/2012WR012514>
- Oakley, J., & O'Hagan, A. (2002). Bayesian inference for the uncertainty distribution of computer model outputs. *Biometrika*, 89(4), 769–784. <https://doi.org/10.1093/biomet/89.4.769>
- O'Loughlin, F. E., Neal, J., Schumann, G. J. P., Beighley, E., & Bates, P. D. (2020). A LISFLOOD-FP hydraulic model of the middle reach of the Congo. *Journal of Hydrology*, 580, 124203. <https://doi.org/10.1016/j.jhydrol.2019.124203>

- Paiva, R. C., Collischonn, W., & Tucci, C. E. (2011). Large scale hydrologic and hydrodynamic modeling using limited data and a GIS based approach. *Journal of Hydrology*, *406*(3–4), 170–181. <https://doi.org/10.1016/j.jhydrol.2011.06.007>
- Pan, F., Xiaohuan, X., & Wang, C. (2020). A comparative study of water indices and image classification algorithms for mapping inland surface water bodies using Landsat imagery. *Remote Sensing*, *12*, 1611. <https://doi.org/10.3390/rs12101611>
- Pappenberger, F., Dutra, E., Wetterhall, F., & Cloke, H. L. (2012). Deriving global flood hazard maps of fluvial floods through a physical model cascade. *Hydrology and Earth System Sciences*, *16*(11), 4143–4156. <https://doi.org/10.5194/hess-16-4143-2012>
- Pinel, S., Bonnet, M. P. S., Da Silva, J., Sampaio, T. C., Garnier, J., Catry, T., et al. (2020). Flooding dynamics within an Amazonian floodplain: Water circulation patterns and inundation duration. *Water Resources Research*, *56*, e2019WR026081. <https://doi.org/10.1029/2019WR026081>
- Rajib, A., Liu, Z., Merwade, V., Tavakoly, A. A., & Follum, M. L. (2020). Towards a large-scale locally relevant flood inundation modeling framework using SWAT and LISFLOOD-FP. *Journal of Hydrology*, *581*, 124406. <https://doi.org/10.1016/j.jhydrol.2019.124406>
- Ramsar. (2007). Ramsar Site Information Service: Zambezi Floodplains. Retrieved from <https://rsis.ramsar.org/rsi/1662>
- Rebelo, L. M., McCartney, M. P., & Finlayson, C. M. (2010). Wetlands of sub-Saharan Africa: Distribution and contribution of agriculture to livelihoods. *Wetlands Ecology and Management*, *18*(5), 557–572. <https://doi.org/10.1007/s11273-009-9142-x>
- River Gauge Data. Retrieved from warma.org.zm/warma-about-us/contact
- Rudorff, C. M., Melack, J. M., & Bates, P. (2014). Flooding dynamics on the lower Amazon floodplain: 1. Hydraulic controls on water elevation, inundation extent, and river-floodplain discharge. *Water Resources Research*, *50*, 619–634. <https://doi.org/10.1002/2013WR014091>
- Rudorff, C. M., Melack, J. M., & Bates, P. D. (2014). Flood dynamics on the lower Amazon floodplain. 1: Hydraulic controls on water elevation, inundation extent, and river-floodplain discharge. *Water Resource Research*, *50*, 619–634. <https://doi.org/10.1002/2013WR014091>
- Sampson, C. C., Smith, A. M., Bates, P. D., Neal, J. C., Alfieri, L., & Freer, J. E. (2015). High resolution global flood hazard model. *Water Resource Research*, *51*, 7358–7381. <https://doi.org/10.1002/2015WR016954>
- Schatz, J. J. (2008). Floods hamper health-care delivery in southern Africa. *Lancet*, *371*(9615), 799–800. [https://doi.org/10.1016/S0140-6736\(08\)60362-1](https://doi.org/10.1016/S0140-6736(08)60362-1)
- Shastry, A., Durand, M., Neal, J., Fernández, A., Phang, S. C., Mohr, B., et al. (2020). Small-scale anthropogenic changes impact floodplain hydraulics: Simulating the effects of fish canals on the Logone floodplain. *Journal of Hydrology*, *588*, 125035. <https://doi.org/10.1016/j.jhydrol.2020.125035>
- Shepard, J. D., Bunting, P., & Dymond, J. R. (2019). Operational large-scale segmentation of imagery based on iterative elimination. *Remote Sensing*, *11*, 658.
- Smith, M. W., Macklin, M. G., & Thomas, C. J. (2013). Hydrological and geomorphological controls of malaria transmission. *Earth-Science Reviews*, *116*, 109–127. <https://doi.org/10.1016/j.earscirev.2012.11.004>
- Stephens, E., Day, J. J., Pappenberger, F., & Cloke, H. (2015). Precipitation and floodiness. *Geophysical Research Letters*, *42*, 10316–10323. <https://doi.org/10.1002/2015GL066779>
- TanDEM Data. Retrieved from <https://tandemx-science.dlr.de/cgi-bin/wcm.pl?page=TDM-Proposal-Submission-Procedure>
- Tan, Z., Li, Y., Xu, X., Yao, J., & Zhang, Q. (2019). Mapping inundation dynamics in a heterogeneous floodplain: Insights from integrating observations and modeling approach. *Journal of Hydrology*, *572*, 148–159. <https://doi.org/10.1016/j.jhydrol.2019.02.039>
- The World Bank. (2010). *The Zambezi river basin: A multi-sector investment opportunities analysis: Volume 3 state of the basin*. World Bank Group
- Tockner, K., & Stanford, J. A. (2002). Riverine flood plains: Present state and future trends. *Environmental Conservation*, *29*(3), 308–330. <https://doi.org/10.1017/s037689290200022x>
- Trigg, M. A., Birch, C. E., Neal, J. C., Bates, P. D., Smith, A., Sampson, C. C., et al. (2016). The credibility challenge for global fluvial flood risk analysis. *Environmental Research Letters*, *11*, 094014. <https://doi.org/10.1088/1748-9326/11/9/094014>
- Trigg, M. A., Wilson, M. D., Bates, P. D., Horritt, M. S., Alsdorf, D. E., Forsberg, B. R., & Vega, M. C. (2009). Amazon flood wave hydraulics. *Journal of Hydrology*, *374*(1–2), 92–105. <https://doi.org/10.1016/j.jhydrol.2009.06.004>
- Ward, P. J., Jongman, B., Weiland, F. S., Bouwman, A., van Beek, R., Bierkens, M. F. P., et al. (2013). Assessing flood risk at the global scale: Model setup, results, and sensitivity. *Environmental Research Letters*, *8*, 044019. <https://doi.org/10.1088/1748-9326/8/4/044019>
- Wessel, B., Huber, M., Wohlfart, C., Marschalk, U., Kosmann, D., & Roth, A. (2018). Accuracy assessment of the global TanDEM-X Digital elevation model with GPS data. *ISPRS Journal of Photogrammetry and Remote Sensing*, *139*, 171–182. <https://doi.org/10.1016/j.isprsjprs.2018.02.017>
- WHO. (2019). *World malaria report 2019* World Health Organization 2019. Licence: CC BY-NC-SA 3.0 IGO.
- Willis, T., Wright, N., & Sleight, A. (2019). Systematic analysis of uncertainty in 2D flood inundation models. *Environmental Modelling & Software*, *122*, 104520. <https://doi.org/10.1016/j.envsoft.2019.104520>
- Wing, O. E. J., Bates, P. D., Sampson, C. C., Smith, A. M., Johnson, K. A., & Erickson, T. A. (2017). Validation of a 30 m resolution flood hazard model of the conterminous United States. *Water Resources Research*, *53*, 7968–7986. <https://doi.org/10.1002/2017WR020917>
- Xu, H.-Q. (2005). A study on information extraction of water body with the modified normalized difference water index (MNDWI). *Journal of Remote Sensing*, *9*(5), 589–595.
- Yamazaki, D., Baugh, C. A., Bates, P. D., Kanae, S., Alsdorf, D. E., & Oki, T. (2012). Adjustment of a spaceborne DEM for use in floodplain hydrodynamic modeling. *Journal of Hydrology*, *436*, 81–91. <https://doi.org/10.1016/j.jhydrol.2012.02.045>
- Yamazaki, D., Ikeshima, D., Tawatari, R., Yamaguchi, T., O'Loughlin, F., Neal, J. C., et al. (2017). A high-accuracy map of global terrain elevations. *Geophysical Research Letters*, *44*, 5844–5853. <https://doi.org/10.1002/2017GL072874>
- Zimba, H., Kawawa, B., Chabala, A., Phiri, W., Selsam, P., Meinhardt, M., & Nyambe, I. (2018). Assessment of trends in inundation extent in the Barotse floodplain, upper Zambezi river basin: A remote sensing-based approach. *Journal of Hydrology: Regional Studies*, *15*, 149–170. <https://doi.org/10.1016/j.ejrh.2018.01.002>